828–836 Nucleic Acids Research, 2012, Vol. 40, No. 2 Published online 28 September 2011
doi:10.1093/nar/gkr767

Structural insights to the metal specificity of an archaeal member of the LigD 3′-phosphoesterase DNA repair enzyme family

Ushati Das, Paul Smith and Stewart Shuman*

Molecular Biology Program, Sloan-Kettering Institute, New York, NY 10065, USA

Received August 4, 2011; Revised August 31, 2011; Accepted September 1, 2011

ABSTRACT

LigD 3′-phosphoesterase (PE) enzymes perform end-healing reactions at DNA breaks. Here we characterize the 3′-ribonucleoside-resecting activity of *Candidatus Korarchaeum* PE. *Cko*PE prefers a single-stranded substrate versus a primer–template. Activity is abolished by vanadate (10 mM), but is less sensitive to phosphate (IC_{50} 50 mM) or chloride (IC_{50} 150 mM). The metal requirement is satisfied by manganese, cobalt, copper or cadmium, but not magnesium, calcium, nickel or zinc. Insights to *Cko*PE metal specificity were gained by solving new 1.5 Å crystal structures of *Cko*PE in complexes with Co^{2+} and Zn^{2+}. His9, His15 and Asp17 coordinate cobalt in an octahedral complex that includes a phosphate anion, which is in turn coordinated by Arg19 and His51. The cobalt and phosphate positions and the atomic contacts in the active site are virtually identical to those in the *Cko*PE·Mn^{2+} structure. By contrast, Zn^{2+} binds in the active site in a tetrahedral complex, wherein the position, orientation and atomic contacts of the phosphate are shifted and its interaction with His51 is lost. We conclude that: (i) PE selectively binds to 'soft' metals in either productive or non-productive modes and (ii) PE catalysis depends acutely on proper metal and scissile phosphate geometry.

INTRODUCTION

Bacterial LigD phosphoesterase (PE) enzymes catalyze manganese-dependent 3′-end-healing reactions at DNA double-strand breaks (DBSs) containing a 3′-phosphate or a 3′-teminal diribonucleotide (1–6). When presented with an all-DNA substrate, bacterial PE acts exclusively as a 3′-phosphomonoesterase to generate a 3′-OH that can serve as a primer for polymerase extension or as a strand donor for ligation. When acting at a 3′-diribonucleotide end, bacterial PE performs two sequential healing steps. First, the terminal nucleoside is removed by a phosphodiesterase activity to yield a primer strand with a ribonucleoside 3′-PO_4 terminus. Then, the 3′-PO_4 is hydrolyzed by a phosphomonoesterase activity to generate a 3′-OH end (Supplementary Figure S1A). The PE enzyme was initially characterized as one of three autonomous catalytic domains—ligase (LIG), polymerase (POL) and PE—that comprise bacterial DNA ligase D (LigD), the central agent of the bacterial non-homologous end-joining (NHEJ) pathway of DSB repair (7). The LigD POL domain adds dNMP or rNMPs at DSB ends and gaps before strand sealing by the LIG domain (8–13). PE trims the short 3′-ribonucleotide tracts produced by POL to generate the 3′-monoribonucleotide ends that are the preferred substrates for sealing by bacterial NHEJ ligases (13).

The crystal structure of the active phosphodiesterase core of *Pseudomonas aeruginosa* PE (*Pae*PE) revealed a novel fold in which an eight-strand β-barrel with a hydrophobic interior supports a distinctive crescent-shaped hydrophilic active site on its outer surface, wherein six essential side chains coordinate manganese and a sulfate mimetic of the scissile phosphate (5). Missing from the *Pae*PE crystal structure was an N-terminal peptide segment, deletion of which selectively diminished the 3′-phosphomonoesterase activity of *Pae*PE without affecting the 3′-phosphodiesterase (2). Protease-sensitivity and solution NMR studies of bacterial PE show that the N-terminal peptide is disordered (2,14).

The detection of stand-alone PE homologs in many bacterial, archaeal and eukaryal proteomes suggests that PEs comprise a new and widely distributed DNA end-healing superfamily (5). To test this idea, we've initiated studies of the activities and structures of two archaeal PE proteins (6). The PE of *Methanosarcina barkeri* (*Mba*PE; 151-aa) conserves the *Pae*PE β-barrel and active site constituents, plus a counterpart of the N-terminal peptide of

*To whom correspondence should be addressed. Tel: 212 639 7145; Fax: 212 717 3623; Email: s-shuman@ski.mskcc.org

bacterial PE. Preliminary characterization showed that *Mba*PE displays both 3′-phosphodiesterase and monoesterase activities *à la* the bacterial LigD PE domains (6). By contrast, the 'minimized' PE of *Candidatus Korarchaeum cryptofilum* (*Cko*PE; 117-aa) comprises the *Pae*PE β-barrel and active site constituents, but lacks a counterpart of the N-terminal peptide of bacterial PE. Preliminary characterization of *Cko*PE showed it to be proficient as a 3′-phosphodiesterase at a DSB end with a 3′-terminal diribonucleotide, but to have relatively feeble phosphomonoesterase activity, similar to the N-terminal deletant of *Pae*PE (6). We recently reported the atomic structures of *Cko*PE and *Mba*PE with Mn^{2+} and a phosphate anion bound in their active sites and identified essential functional groups by structure-guided mutagenesis (6). Concordance of mutational effects on phosphodiesterase activity in archaeal and bacterial PEs suggested conservation of the PE catalytic mechanism. A notable sidebar to the *Mba*PE structure was that the N-terminal peptide segment, though present in the crystal, was invisible in the electron density.

The high resolution of the *Cko*PE crystal structure (1.1 Å) recommends *Cko*PE as a model for further mechanistic studies of the PE family and for efforts to capture crystallographic snapshots of PE enzymes along the phosphodiesterase reaction pathway. In the present study, we examine the substrate preference, reaction optima and metal cofactor specificity of *Cko*PE. Prompted by our findings, we determined new crystal structures of the enzyme in complexes with cobalt and zinc, which exemplify catalytically productive and non-productive states of metal and phosphate binding, respectively.

MATERIALS AND METHODS

Assay of PE activity

The 3′-diribonucleotide-containing substrates used in the 3′-PE assays were 5′ ^{32}P-labeled and gel-purified. Where indicated, the labeled single-stranded oligonucleotides were annealed to a 4-fold molar excess of an unlabeled complementary DNA strand to form a primer–template structure. PE reaction mixtures (10 µl) contained 50 mM Tris–HCl (pH 7.5), 0.5 mM $MnCl_2$, 0.5 pmol 5′ ^{32}P-labeled substrate and *Cko*PE as specified. The reactions were quenched by adding 5 µl of 90% formamide, 50 mM EDTA, 0.1% bromophenol blue. The samples were analyzed by electrophoresis through a 15-cm 24% polyacrylamide gel or a 40-cm 18% polyacrylamide gel containing 8 M urea in 0.45 mM Tris–borate, 1.2 mm EDTA. The radiolabeled products were visualized by autoradiography. The extents of reaction were quantified by scanning the gel with a Fujix BAS2500 imager.

Crystallization, X-ray diffraction and structure determination

The tag-free *Cko*PE protein was purified as described previously (6). Crystallization was performed by hanging-drop vapor diffusion at 22°C. Solutions of 0.7 mM *Cko*PE and 10 mM $CoCl_2$ or $ZnCl_2$ were mixed 1:1 with, and then equilibrated against, a reservoir solution of 0.2 M Na_2HPO_4 and 20% PEG-3350. Crystals grew overnight and were cryoprotected with reservoir solution containing 10% ethylene glycol prior to flash freezing in liquid nitrogen. Separate strategies were used for collecting data employed in structure refinement and data used to confirm the identity of the metal complexed with the protein, as follows.

Diffraction data for structure determination of each *Cko*PE•metal complex were collected at NSLS beamline X25 equipped with a Pilatus 6 M detector. The data set comprised 370 oscillations of 0.5° each. The data were integrated and reduced with MOSFLM and SCALA (15). Diffraction statistics are compiled in Table 1. Structures of the *Cko*PE•Co^{2+} and *Cko*PE•Zn^{2+} complexes were determined by refining against the *Cko*PE•Mn^{2+} structure (PDB ID 3P4H) with cobalt or zinc in place of manganese. Manual rebuilding was done using COOT (16), after which the models were refined in PHENIX (17) using standard procedures. Refinement statistics are compiled in Table 1.

For the analysis of metal identity, a single crystal of each *Cko*PE•metal complex was used to collect three complete and highly redundant datasets (at NSLS beamline X25 equipped with an ADSC-Q315 CCD detector) at three different wavelengths using either short exposure times (<0.5 s) or beam attenuators to minimize radiation damage. The wavelengths were chosen in order to optimize the anomalous scattering for each metal presumed to be present in the crystal. For the zinc complex, complete datasets were collected at 1.2833, 1.2837 and 1.8990 Å, corresponding to the peak and inflection energies of the K-edge absorption for zinc and the peak absorption energy for manganese, respectively. For the cobalt complex, datasets were collected at 1.6079, 1.6093 and 1.2836 Å, corresponding to the peak and inflection energies of the K-edge absorption for cobalt and the peak absorption energy for zinc, respectively. Exact beamline energies were determined by measuring the fluorescence spectra of precipitant solutions containing 2 mM manganese, 10 mM cobalt and 10 mM zinc and correlating observed maxima with the energy setting of the monochromator. The presence of cobalt or zinc in the *Cko*PE crystals was confirmed by in situ fluorescence scanning of each crystal prior to data collection. The confirmation that the metal present in the crystal sample was, in fact, present at the active site was conducted as follows. Phases from the previous *Cko*PE•Mn^{2+} model were used to create anomalous difference Fourier maps of each metal complex. For both zinc and cobalt, only a single large peak was present in the resulting map. For each complex, the corresponding metal was placed at the peak of the anomalous difference map and the resulting structure was refined in PHENIX. In conjunction with this refinement, the anomalous scattering factors for each metal were refined against observed Bijvoet differences (compiled in Table 2).

Table 1. Crystallographic data and refinement statistics

	*Cko*PE•Zn^{2+}	*Cko*PE•Co^{2+}
Space group	$P2_1$	$P2_1$
Unit cell dimensions @ 130 K	a = 27.7 Å, b = 58.6 Å, c = 33.0 Å, β = 102.4°	a = 27.7 Å, b = 58.4 Å, c = 33.1 Å, β = 102.6°
Radiation Source	NSLS-X25	NSLS-X25
Wavelength, Å	1.282	1.282
Crystallographic Data Quality		
Resolution, Å	32.21–1.48 (1.56–1.48)	28.24–1.52 (1.60–1.52)
R_{sym}, %	2.8 (6.0)	3.8 (7.7)
Unique Reflections	16 869 (2227)	15 703 (2173)
Mean Redundancy	2.8 (2.1)	3.0 (2.6)
Completeness, %	97.9 (89.1)	98.8 (94.5)
Mean I/σI	16.8 (8.6)	17.7 (8.6)
Refinement and Model Statistics, $F > \sigma F$		
Resolution, Å	29.3–1.48 (1.53–1.48)	24.6–1.52 (1.57–1.52)
Completeness, %	98.9 (84.8)	99.7 (92.0)
R_{free}/R_{work}, %	18.0/14.7 (23.8/18.5)	18.7/15.7 (25.3/18.8)
RMS Deviation for Bonds Lengths	0.0129 Å	0.0092 Å
RMS Deviation for Bonds Angles	1.491°	1.297°
Ramachandran plot	98.4% favored; no outliers	98.4% favored; no outliers
B-factors, $Å^2$ Wilson / Overall	11.7 / 17.0	12.5 /16.2
Model Contents		
Amino acid residues	118	118
Heteroatoms	1 PO_4, 1 Zn, 1 PEG	1 PO_4, 1 Co, 1 PEG
Waters	207	203
PDB ID	3TA7	3TA5

Standard definitions are used for all of the parameters. Figures in parentheses refer to data in the highest resolution bin. The refinement and geometric statistics come from PHENIX. R_{sym} output as R_{merge} by MOSFLM. R_{free} sets for cross validation consisted of 5% of data selected at random against which structures were not refined.

Table 2. Refinement of anomalous scattering factors

	λ (Å)	eV	f′ (obs)	f′ (calc)	f″ (obs)	f″ (calc)
*Cko*PE•Zn^{2+}	1.2833	9661.3	–5.39	–8.10	4.17	3.97
	1.2837	9658.4	–6.33	–8.01	2.44	2.13
	1.8990	6536.8	–2.28	–0.96	0.78	1.00
*Cko*PE•Co^{2+}	1.6079	7711.0	–5.04	–8.17	5.01	3.97
	1.6093	7704.2	–6.70	–7.46	2.59	0.45
	1.2836	9641.8	–0.52	–0.41	2.35	2.73

Observed values for f′ and f″ were determined by refinement of anomalous scattering factors for a single atom placed at the active site against observed Bijvoet differences. Calculated values are compared from the http://skuld.bmsc.washington.edu/scatter/website.

RESULTS AND DISCUSSION

Substrate preference of *Cko*PE

*Cko*PE was reacted with a 5′ ^{32}P-labeled 24-mer substrate (D22R2) composed of 22 deoxynucleotides linked to a 3′-terminal diribonucleotide, or with a primer–template substrate formed by annealing the labeled D22R2 strand to a 4-fold molar excess of a complementary 36-mer all-DNA strand (Figure 1). The extents of 3′-processing during 30 min incubation at 37°C were measured as a function of input *Cko*PE (Figure 1). In both cases, the D22R2 species was converted in a PE concentration-dependent manner to a mixture of two products: (i) a predominant species D22R1p, the immediate product of the 3′-phosphodiesterase reaction; and (ii) a minor species $D22R1_{OH}$, derived from D22R1p via the relatively feeble phosphomonoesterase activity of *Cko*PE (Supplementary Figure S1B). The specific activity of *Cko*PE with the single-stranded D22R2 substrate was 4-fold greater than that with the primer–template (Figure 1). Virtually all of the input D22R2 strand was processed at saturating levels of *Cko*PE. The product distribution (~90% D22R1p and ~10% $D22R1_{OH}$) did not vary significantly with *Cko*PE concentration or the presence of the complementary template strand (data not shown). A control experiment was performed in which we supplemented the D22R2 substrate with a 4-fold molar excess of a 36-mer homo-oligodeoxyadenylate strand. We found that the dA36 strand did not affect the specific activity of *Cko*PE (Figure 1). Thus, we conclude that the decrement in activity between the single-stranded and primer–template substrates reflects suppressive effects of duplex secondary structure. The preference of the *Cko*PE phosphodiesterase for single-stranded 3′-diribonucleotide substrates is in contrast to *Pae*PE, which is several fold more active as a phosphodiesterase on a primer–template than on a single-stranded substrate (1).

Effect of temperature

The preference for single-stranded substrates facilitated analysis of the temperature-dependence of 3′-processing by *Cko*PE. The kinetics of 3′-processing of the D22R2 single-strand by a 25-fold molar excess of *Cko*PE at 37°C and 55°C are shown in Figure 2. The data fit well to a single exponential with apparent rate constants of $0.18\,min^{-1}$ at 37°C and $0.26\,min^{-1}$ at 55°C. The apparent rate constants at other temperatures were as follows: $0.22\,min^{-1}$ at 65°C; $0.25\,min^{-1}$ at 45°C; and $0.05\,min^{-1}$ at 23°C (data not shown). Activity at

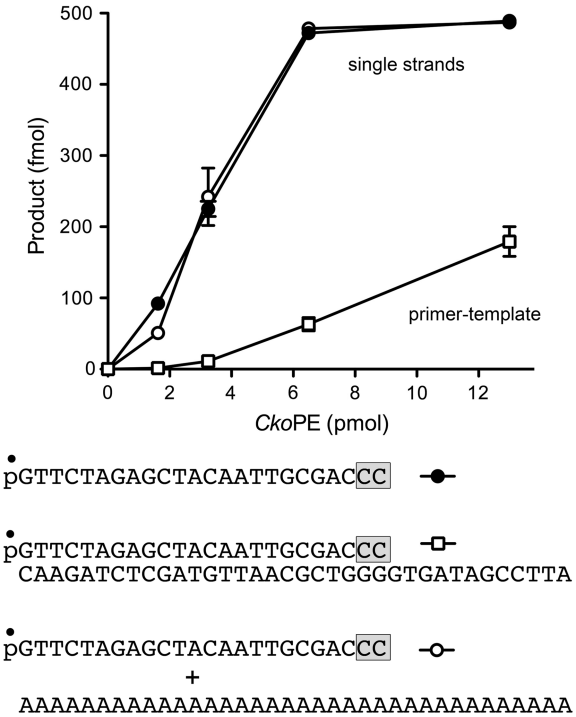

Figure 1. *Cko*PE prefers a single stranded substrate versus a primer template. PE reaction mixtures (10 µl) containing 50 mM Tris–HCl (pH 7.5), 0.5 mM $MnCl_2$, 500 fmol ^{32}P-labeled substrate as specified and increasing amounts of *Cko*PE were incubated for 30 min at 37°C. The products were resolved by urea–PAGE and visualized by autoradiography. Product formation was quantified and plotted as a function of input *Cko*PE. Each datum is the average of three independent experiments (±SEM). Substrates are shown below the graph, with the 5′-^{32}P-label (p) indicated by filled circle and the ribonucleotides highlighted in shaded boxes.

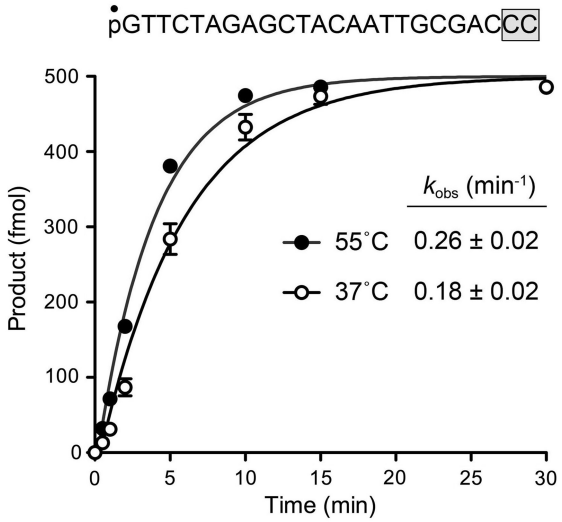

Figure 2. Single-turnover kinetics. PE reaction mixtures containing 50 mM Tris–HCl (pH 7.5), 0.5 mM $MnCl_2$, 50 nM ^{32}P-labeled D22R2 substrate (shown above the graph) and 1.25 µM *Cko*PE were incubated at 37°C or 55°C. Aliquots (10 µl, containing 500 fmol of substrate) were withdrawn at 0.5, 1, 2, 5, 10, 15 and 30 min and quenched immediately. The time 0 sample was withdrawn prior to adding *Cko*PE. The products were resolved by urea–PAGE and visualized by autoradiography. Each datum is the average of three independent experiments (±SEM). Apparent rate constants were calculated by non-linear regression fitting of the data to a one-phase association function in PRISM.

elevated temperatures is consistent with the thermophilic growth properties of *Candidatus Korarchaeum cryptofilum* (18). *Cko*PE activity on the D22R2 substrate at 37°C displayed a broad and flat pH optimum from pH 5.5 to 9.0 in 50 mM Tris–acetate or Tris–HCl buffers (data not shown). Activity was virtually abolished at pH 4.5 and 10.0 (data not shown).

Effect of substrate length

We incrementally trimmed the D22R2 substrate from its 5′-end to yield 12-mer (D10R2) and 6-mer (D4R2) strands with the same 3′-nucleotide sequence and diribonucleotide termini (Figure 3). We compared them at equimolar concentrations as substrates for *Cko*PE. Shortening the substrate from 24 to 12 nt elicited a 2- to 3-fold decrement in specific activity (Figure 3), though processing of D10R2 proceeded to near completion at the highest enzyme levels tested and the product distribution (predominated by D10R1p) was similar to that seen with the 24-mer substrate. A more drastic decline in activity was seen when the substrate was shortened to a 6-mer, to wit, the specific activity with D4R2 was 28-fold lower than that with D22R2 and the yield of processed ends did not exceed 10% of the input substrate at the highest enzyme levels tested (Figure 3). These results suggest that *Cko*PE engages the oligonucleotide substrate at some distance from the 3′-diribonucleotide terminus at which PE chemistry occurs.

Inhibition by anions

Available crystal structures of bacterial and archaeal PE proteins are notable for the presence of an oxyanion (either phosphate or sulfate) in the active site (5,6). We presume that the oxyanion occupies the site at which the scissile phosphodiester is engaged, in which case suitable inorganic anions might compete with substrate binding and inhibit *Cko*PE activity. Here we tested the effects of increasing concentrations of sodium chloride, sodium phosphate and sodium vanadate on 3′-resection of the D22R2 substrate. Chloride was a relatively weak inhibitor, with an IC_{50} of ~150 mM (Figure 4). Phosphate was a better inhibitor than chloride, with an IC_{50} of ~50 mM (Figure 4). Vanadate was considerably more potent; 10 mM vanadate reduced product formation to <1% of the control value (Figure 4). The hierarchy of inhibition suggests non-specific electrostatic effects of chloride on *Cko*PE binding to the oligonucleotide backbone, more selective effects of phosphate anion competing with substrate for binding to the *Cko*PE active site, and even more avid binding by vanadate as a putative transition-state mimetic owing to its capacity for adoption of trigonal bipyramidal geometry (19).

Divalent cation specificity

The 3′-processing activity of *Cko*PE with the D22R2 single-stranded substrate was strictly dependent on a

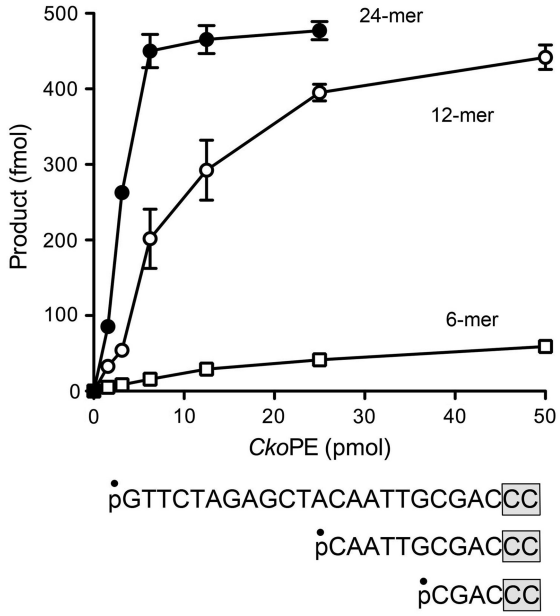

Figure 3. Influence of substrate length on *Cko*PE activity. PE reaction mixtures (10 µl) containing 50 mM Tris–HCl (pH 7.5), 0.5 mM $MnCl_2$, 500 fmol ^{32}P-labeled 24-mer, 12-mer or 6-mer single stranded substrates and *Cko*PE as specified were incubated for 30 min at 37°C. The products were analyzed by urea–PAGE and visualized by autoradiography. Extents of conversion were quantified and plotted as a function of input *Cko*PE. Each datum is the average of three independent experiments (±SEM). Substrates are shown below the graph, with the 5′-^{32}P-label (p) indicated by filled circle and the ribonucleotides highlighted in shaded boxes.

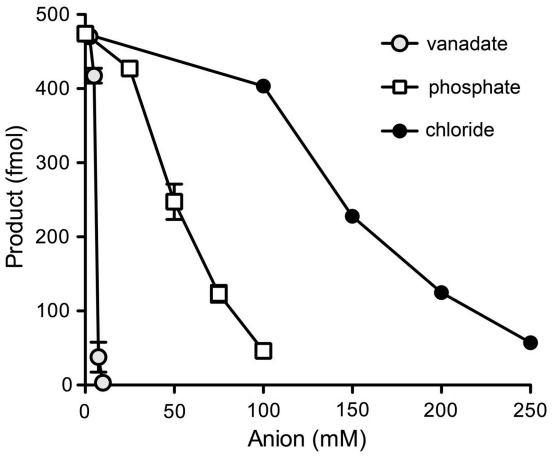

Figure 4. Inhibition by anions. PE reaction mixtures (10 µl) containing 50 mM Tris–HCl (pH 7.5), 0.5 mM $MnCl_2$, 500 fmol ^{32}P-labeled D22R2 substrate, 6 pmol *Cko*PE and sodium vanadate, sodium phosphate, or sodium chloride as indicated were incubated for 30 min at 37°C. The stock solution (100 mM) of activated sodium vanadate was prepared by dissolving sodium orthovanadate (Sigma) in water, heating the solution for 5 min at 90°C and then adjusting the pH to 10.0–10.5 with NaOH, at which point the solution was clear and colorless. Addition of 1 µl of the vanadate stock to the PE reaction mixture to achieve the highest final concentration tested in this experiment (10 mM vanadate) elicited a slight increase in the pH of the reaction mixture (to pH 8.0), which does not affect PE activity *per se*. Extents of product formation are plotted as a function of anion concentration. Each datum is the average of three independent experiments (±SEM).

divalent cation cofactor. The metal requirement was satisfied by 0.5 mM manganese, cobalt, copper or cadmium (Figure 5A). Magnesium, nickel and zinc were ineffective, and calcium was only weakly active (Figure 5A). The metal specificity seen here was broader than that reported previously for *Cko*PE activity with a primer–template substrate, which was dependent on manganese and was ineffective in the presence of cobalt, copper and cadmium (6). We suspect this difference might be attributable to adverse effects of cobalt, copper and cadmium on *Cko*PE recognition of a duplex substrate (conceivably by altering its conformation or electrostatics) that do not apply to the preferred single-stranded substrate. Additional insights to the metal specificity of *Cko*PE with the D22R2 single-strand were provided by mixing experiments, in which reaction solutions containing 0.5 mM manganese were supplemented with 0.5 mM of each of the series of divalent cations. Nickel and zinc inhibited PE activity in the presence of manganese (data not shown), suggesting that these metals might compete with manganese for a putative metal-binding site on the enzyme, wherein engaged they are unable to support reaction chemistry. Titration of zinc against 0.5 mM manganese revealed a concentration-dependent inhibition with an IC_{50} of ~75 µM, suggesting that *Cko*PE has a higher affinity for zinc than manganese. Other metals that were ineffective per se (e.g. magnesium and calcium) had no such deleterious effect in combination with manganese (data not shown), suggesting that magnesium and calcium do not bind avidly to the *Cko*PE active site.

Crystallization of *Cko*PE in complexes with cobalt and zinc

To gain better insights to the distinctive metal specificity of *Cko*PE, we attempted to grow crystals of the protein after pre-mixing with various divalent cations that either supported catalytic activity (cobalt) or inhibited activity in the presence of manganese (zinc and nickel). Crystals of *Cko*PE•Co^{2+} and *Cko*PE•Zn^{2+} grew overnight by vapor diffusion against a precipitant solution containing PEG-3350 and 0.2 M sodium phosphate. (We were unsuccessful in crystallizing *Cko*PE in the presence of magnesium, calcium, copper, nickel or cadmium under these conditions.) Diffraction data at ~1.5 Å resolution were collected for *Cko*PE•Co^{2+} and *Cko*PE•Zn^{2+} crystals in space group $P2_1$. The structures were solved by refinement against the 1.1 Å *Cko*PE•Mn^{2+} structure reported previously (6). The diffraction data statistics and refinement statistics are compiled in Table 1. The tertiary structure of *Cko*PE•Co^{2+} and *Cko*PE•Zn^{2+} were extremely similar to one another (rmsd of 0.09 Å at all Cα positions) and also to *Cko*PE•Mn^{2+} (rmsds of 0.15 Å at all Cα positions for *Cko*PE•Co^{2+} versus *Cko*PE•Mn^{2+} and 0.19 Å at all Cα positions for *Cko*PE•Zn^{2+} versus *Cko*PE•Mn^{2+}). The salient features of the two new structures pertain to their active sites.

The electron density map for the *Cko*PE•Co^{2+} active site (Figure 6A) highlights an octahedral coordination

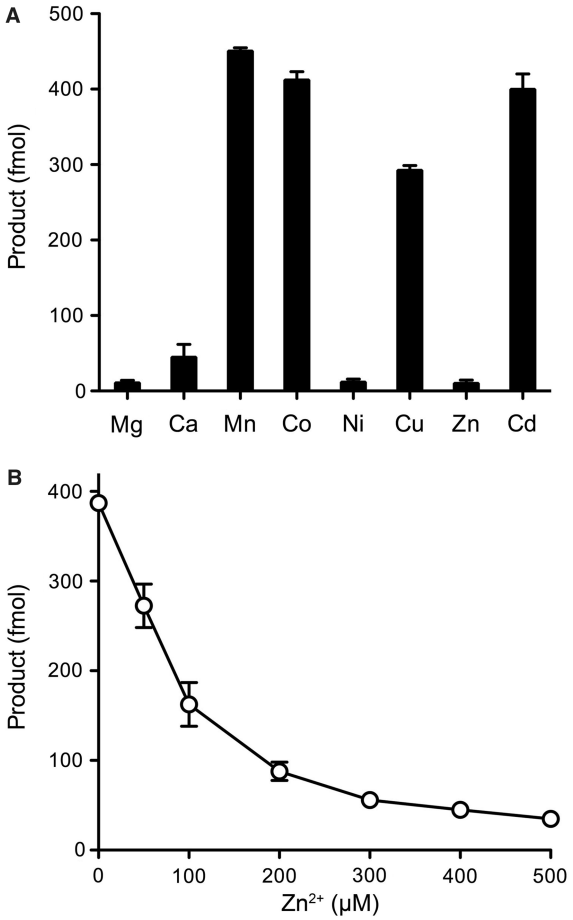

Figure 5. Divalent cation specificity of *Cko*PE. (**A**) PE reaction mixtures (10 μl) containing 50 mM Tris–HCl (pH 7.5), 500 fmol ^{32}P-labeled 24-mer single stranded substrate, 6 pmol *Cko*PE and 0.5 mM of the indicated divalent cations were incubated for 20 min at 37°C. The reactions were quenched with EDTA/formamide. The products were analyzed by urea–PAGE and visualized by autoradiography. Extents of conversion were quantified and plotted in bar graph format. Each datum is the average of three independent experiments (±SEM). (**B**) PE reaction mixtures (10 μl) containing 50 mM Tris–HCl (pH 7.5), 0.5 mM $MnCl_2$, 500 fmol ^{32}P-labeled 24-mer single stranded substrate, 3 pmol *Cko*PE and increasing concentrations of $ZnCl_2$ as specified were incubated for 20 min at 37°C. Product formation is plotted as a function of input Zn^{2+}. Each datum is the average of three independent experiments (±SEM).

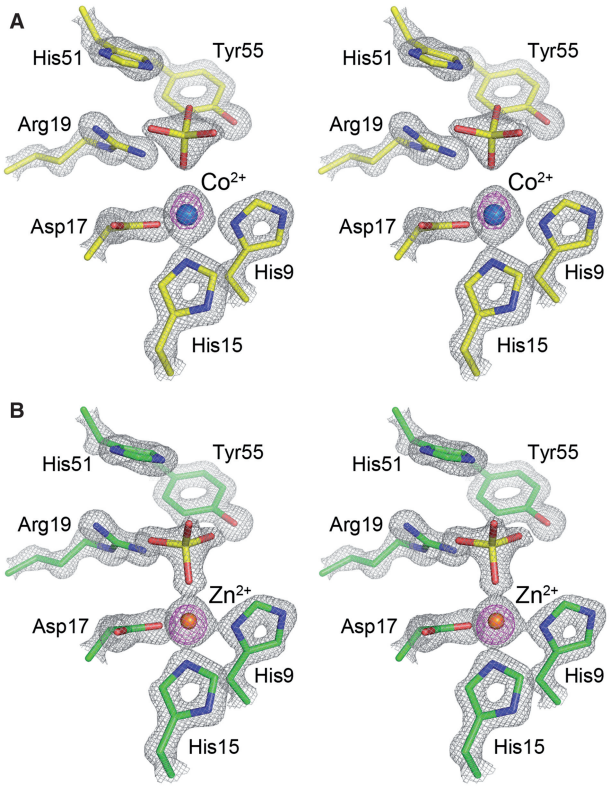

Figure 6. *Cko*PE•Co^{2+} and *Cko*PE•Zn^{2+} active site electron density. Stereo views of 2*fo*–*fc* density maps of the *Cko*PE•Co^{2+} (panel A) and *Cko*PE•Zn^{2+} (panel B) active sites contoured at 2σ (gray mesh). The magenta mesh is the anomalous difference density for the cobalt and zinc ions contoured at 20σ.

complex about the cobalt ion, which is rendered as a blue sphere surrounded by its 20σ anomalous difference density. Adjacent to the metal ion is a tetrahedral density corresponding to phosphate anion. The cobalt ligands are His9-Nδ, His15-Nε, Asp17-Oε and a phosphate oxygen (Figure 6A), plus two waters (Supplementary Figure S2A and Figure 7, middle panel). The phosphate is bound in the active site via its atomic contacts to cobalt, the essential side chains Arg19 and His51, and a water-bridged contact to Tyr55 (Figure 7, middle panel). The instructive point is that the metal and phosphate positions and the atomic contacts in the active site are virtually identical in the *Cko*PE•Mn^{2+} and *Cko*PE•Co^{2+} structures (Figure 7, compare top and middle panels). Thus, the 'good' metals manganese and cobalt have a common productive binding mode to the *Cko*PE active site.

By contrast, Zn^{2+} (rendered as an orange sphere in Figure 6B and Supplementary Figure S2B) binds in the active site at the center of a tetrahedral coordination complex with His9, His15, Asp17 and phosphate anion (Figure 7, bottom panel). Moreover, the position, orientation and atomic contacts of the phosphate anion are shifted in the *Cko*PE•Zn^{2+} active site compared to the manganese and cobalt complexes (Figure 7, bottom panel). For example, whereas Arg19, Tyr55 and the metal ion contact the same phosphate oxygen in the *Cko*PE•Mn^{2+} and *Cko*PE•Co^{2+} structures, these three ligands engage three different phosphate oxygens in the *Cko*PE•Zn^{2+} active site (Figure 7). In addition, the interaction of the phosphate with the essential His51 side chain (seen in *Cko*PE•Mn^{2+} and *Cko*PE•Co^{2+}) is lost in the *Cko*PE•Zn^{2+} active site (Figure 7).

To verify the metal assignments in the active sites of the two new structures reported here, we collected diffraction data at three additional wavelengths chosen in order to optimize the anomalous scattering for each metal presumed to be present in the *Cko*PE crystal. The anomalous scattering factors for the active site metals were refined against the observed Bijvoet differences (Table 2). In the case of *Cko*PE•Zn^{2+} complex, the values for f″ dropped by roughly half when refined

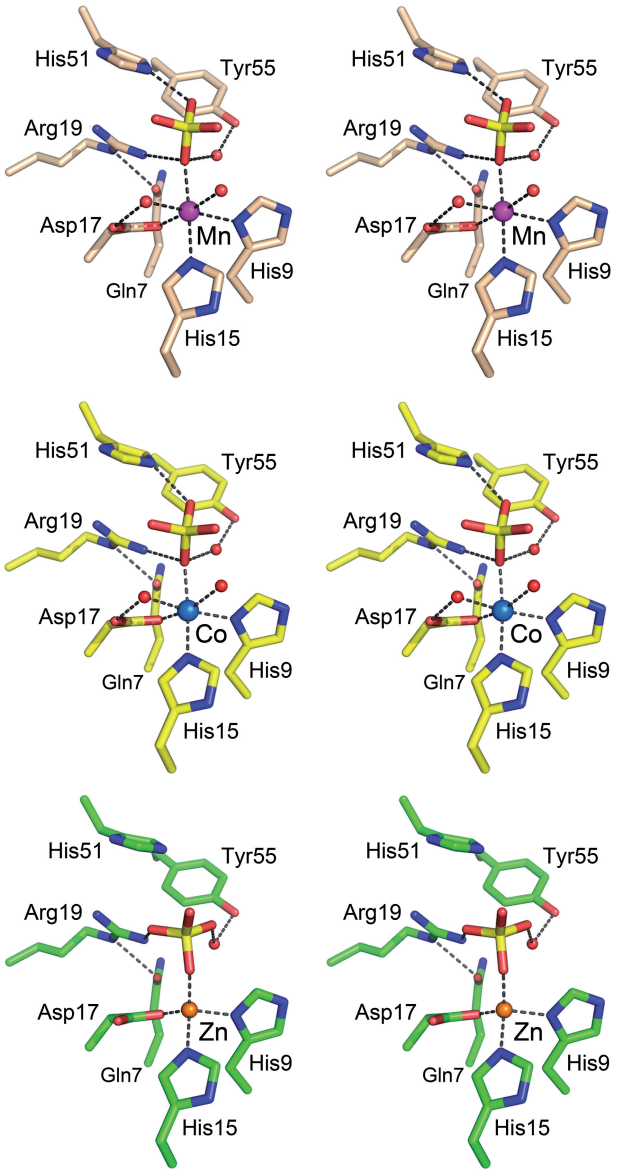

Figure 7. Comparison of the *Cko*PE active sites in complex with manganese, cobalt and zinc. Stereo views of the active sites of *Cko*PE·Mn^{2+} (top panel), *Cko*PE·Co^{2+} (middle panel) and *Cko*PE·Zn^{2+} (bottom panel). Selected amino acid side-chain atoms are rendered as stick models. A phosphate anion (a putative mimic of the scissile phosphate) is shown as a stick model. Manganese, cobalt and zinc are depicted as magenta, cyan and orange spheres, respectively. Waters are shown as red spheres. Interatomic contacts are indicated by dashed lines.

against data collected at energies corresponding to a theoretical x-ray absorption maximum and inflection for zinc (1.2833 Å and 1.2837 Å, respectively), though these energies differ by only a few electron volts (eV). Because these transitions are atom-specific, the observation of such a change suggests that the anomalous scatterer observed at the active site of the complex was, in fact, zinc. Similarly, the refined values for the dispersive differences (f′) for zinc at each of these two wavelengths were consistent with theoretical values for zinc (Table 2). Furthermore, the relatively low value for f″ observed for the zinc complex collected at the manganese absorption peak (1.899 Å) is entirely in line with the theoretical scattering for zinc at this wavelength and dismisses the possibility of any significant co-occupancy of the active site by manganese in the zinc complex structure.

For the *Cko*PE·Co^{2+} complex, a sharp drop in f″ was observed when refining data collected at the theoretical cobalt peak and inflection energies (1.6079 Å and 1.6093 Å, respectively), indicative of cobalt being present in the complex (Table 2). Likewise, refined values for f′ at these wavelengths are consistent with cobalt. Lastly, the value for f″ observed for the cobalt complex at the zinc absorption maximum precludes the presence of zinc at the active site of this complex (Table 2).

CONCLUSION

Our biochemical and structural analyses show that: (i) *Cko*PE selectively binds to 'soft' metals in either productive (manganese, cobalt) or non-productive (zinc) modes; and (ii) *Cko*PE catalysis depends acutely on a proper metal and scissile phosphate geometries. The conservation of tertiary structure and active site architecture in archaeal and bacterial PEs suggests that the good-metal/bad-metal dichotomy applies generally to the PE superfamily, all of which are manganese-dependent and none of which are active with zinc (2,4). The present study fortifies the prediction of a common catalytic mechanism for the phosphodiesterase step via transition state stabilization by the metal and by essential arginine and histidine side chains. The tetrahedral coordination of zinc in the active site results in a subtle but significant distortion of the phosphate orientation and contacts, especially the severance of the phosphate contact to an essential histidine. Selectivity for manganese over magnesium is a shared feature of archaeal and bacterial PEs. We have suggested that this preference is attributable to the soft metal contacts with histidine nitrogens at two of the six positions of the productive octahedral coordination complex.

The present findings add to a growing appreciation of the role of manganese in DNA repair and clastogen resistance (20). With respect to the bacterial NHEJ enzymes, manganese (or cobalt) serves as the essential cofactor for the catalytic activity of the POL module of LigD (magnesium being ineffective or less effective for LigD POL activity *in vitro*) (4,8), and manganese is the preferred cofactor (over magnesium) for the strand sealing activity of the bacterial NHEJ ligases (4). The crystal structure of the LigD POL domain bound to a nucleoside triphosphate substrate revealed two manganese ions in the active site, in complete and partially filled octahedral coordination complexes with three essential carboxylate side chains and the NTP phosphate oxygens (9). Thus, the selectivity of the LigD POL for manganese (or cobalt) over magnesium is not explained by reliance on soft amino acid metal ligands. The structure of the LigD LIG domain suggests that carboxylates are the likely metal ligands (21), as they are for all other ligases that utilize magnesium as the preferred cofactor. At this point, it is not clear why bacterial NHEJ ligases prefer manganese over magnesium,

though we suspect it may relate to their distinctive preference for sealing broken nucleic acids with 3′-monoribonucleotide ends (13). Other instances of strong manganese preference have been described for polynucleotide ligases from *Deinococcus radiodurans* (22,23), an organism that depends on manganese for its resistance to oxidative damage (20). The exonuclease Mre11, a key player in DNA recombination, and the RNA 3′-end-healing enzyme *Cth*Pnkp, are also manganese-dependent (24,25), consistent with the fact that Mre11 and the 3′-phosphoesterase module of *Cth*Pnkp belong to the binuclear metallophosphoestease superfamily, defined by a common fold and metal-binding site entailing octahedral coordination of the metals to three histidine side chains (26,27).

Our characterization of *Cko*PE raises several questions about its contributions to DNA repair and the prospects of regulation by metal availability. Whereas the bacterial PE proteins and many of the stand-alone archaeal PEs have a conserved N-terminal peptide that confers vigorous 3′-phosphomonoesterase activity in addition to the 3′-ribonucleoside-resecting phosphodiesterase, *Cko*PE lacks the N-domain and is a feeble 3′-phosphomonoesterase. Thus, for *Cko*PE to provide a full end-healing function on a DNA substrate containing 3′-ribonucleotides, it must either be assisted by a second enzyme with 3′-phosphomonoesterase activity, or have 3′-phosphomonoesterase activity conferred on the core PE fold by interaction with a hypothetical regulatory protein (i.e. that acts as a functional analog of the N-terminal peptide of other PEs). It is conceivable that the 3′-phosphodiesterase of *Cko*PE acts on termini other than a 3′-diribonucleotide (e.g. damaged ends) that might be relevant to end-healing. Our findings that non-productive binding of zinc to the PE active site can compete with the productive binding of manganese and thereby suppress PE activity (quite effectively when both metals are at equal concentration) prompts the question of how PE enzymes acquire a good metal *in vivo*. Import or intracellular mobilization of manganese under conditions of genotoxic stress (20) is a potential means to ensure that manganese-dependent repair functions are available when needed. There is clearly more to learn about the physiology of the PE enzyme family, though significant obstacles are imposed by the lack of well-developed genetics in the archaeal taxa that have PE proteins and the lack of specific assays for 3′-end-healing *in vivo* (28) in the PE-encoding bacteria that are tractable genetically.

ACCESSION NUMBERS

PDB 3TA5, 3TA7.

SUPPLEMENTARY DATA

Supplementary Data are available at NAR Online: Supplementary Figures S1 and S2.

ACKNOWLEDGEMENTS

S.S. is an American Cancer Society Research Professor. The NSLS beamline is supported by the Offices of Biological and Environmental Research and of Basic Energy Sciences of the US Department of Energy, and the National Center for Research Resources of the National Institutes of Health.

FUNDING

Funding for open access charge: National Institutes of Health (grant GM63611).

Conflict of interest statement. None declared.

REFERENCES

1. Zhu,H. and Shuman,S. (2005) Novel 3′-ribonuclease and 3′-phosphatase activities of the bacterial non-homologous end-joining protein, DNA ligase D. *J. Biol. Chem.*, **280**, 25973–25981.
2. Zhu,H., Wang,L.K. and Shuman,S. (2005) Essential constituents of the 3′-phosphoesterase domain of bacterial DNA ligase D, a nonhomologous end-joining enzyme. *J. Biol. Chem.*, **280**, 33707–33715.
3. Zhu,H. and Shuman,S. (2006) Substrate specificity and structure-function analysis of the 3'-phosphoesterase component of the bacterial NHEJ protein, DNA Ligase D. *J. Biol. Chem.*, **281**, 13873–13881.
4. Zhu,H. and Shuman,S. (2007) Characterization of *Agrobacterium tumefaciens* DNA ligases C and D. *Nucleic Acids Res.*, **35**, 3631–3645.
5. Nair,P.A., Smith,P. and Shuman,S. (2010) Structure of bacterial LigD 3′-phosphoesterase unveils a DNA repair superfamily. *Proc. Natl Acad. Sci. USA*, **107**, 12822–12827.
6. Smith,P., Nair,P.A., Das,U., Zhu,H. and Shuman,S. (2011) Structures and activities of archaeal members of the LigD 3′-phosphoesterase DNA repair enzyme superfamily. *Nucleic Acids Res.*, **39**, 3310–3320.
7. Shuman,S. and Glickman,M.S. (2007) Bacterial DNA repair by non-homologous end joining. *Nature Rev. Microbiol.*, **5**, 852–861.
8. Zhu,H. and Shuman,S. (2005) A primer-dependent polymerase function of *Pseudomonas aeruginosa* ATP-dependent DNA ligase (LigD). *J. Biol. Chem.*, **280**, 418–427.
9. Zhu,H., Nandakumar,J., Aniukwu,J., Wang,L.K., Glickman,M.S., Lima,C.D. and Shuman,S. (2006) Atomic structure and NHEJ function of the polymerase component of bacterial DNA ligase D. *Proc. Natl Acad. Sci. USA*, **103**, 1711–1716.
10. Zhu,H. and Shuman,S. (2010) Gap filling activities of *Pseudomonas* LigD polymerase and functional interactions of LigD with the DNA end-binding Ku protein. *J. Biol. Chem.*, **285**, 4815–4825.
11. Pitcher,R.S., Brissett,N.C., Picher,A.J., Andrade,P., Juarez,R., Thompson,D., Fox,G.C., Blanco,L. and Doherty,A.J. (2007) Structure and function of a mycobacterial NHEJ DNA repair polymerase. *J. Mol. Biol.*, **366**, 391–405.
12. Brissett,N.C., Pitcher,R.S., Juarez,R., Picher,A.J., Green,A.J., Dafforn,T.R., Fox,G.C., Blanco,L. and Doherty,A.J. (2007) Structure of a NHEJ polymerase-mediated synaptic complex. *Science*, **318**, 456–459.
13. Zhu,H. and Shuman,S. (2008) Bacterial nonhomologous end joining ligases preferentially seal breaks with a 3′-OH monoribonucleotide. *J. Biol. Chem.*, **283**, 8331–8339.
14. Dutta,K., Natarajan,A., Nair,P.A., Shuman,S. and Ghose,R. (2011) Sequence-specific ^{1}H, ^{13}C and ^{15}N assignments of the phosphoesterase (PE) domain of *Pseudomonas aeruginosa* DNA ligase D (LigD). *Biomolecular NMR Assignments*, **5**, 151–155.
15. Leslie,A.G.W. (1992) Recent changes to the MOSFLM package for processing film and image plate data. *Joint CCP4 + ESF-EAMCB Newslett, Protein Crystallogr.*, **26**

16. Emsley,P. and Cowtan,K. (2004) Coot: model-building tools for molecular graphics. *Acta Crystallogr.*, **D60**, 2126–2132.
17. Adams,P.D., Grosse-Kunstleve,R.W., Hung,L.W., Ioerger,T.R., McCoy,A.J., Moriarty,N.W., Read,R.J., Sacchettini,J.C., Sauter,N.K. and Terwilliger,T.C. (2002) PHENIX: building new software for automated crystallographic structure determination. *Acta Crystallogr.*, **D58**, 1948–1954.
18. Elkins,J.G., Podar,M., Graham,D.E., Makarova,K.S., Wolf,Y., Randua,L., Hedlund,B.P., Brochier-Armanet,C., Kunin,V., Anderson,I. *et al.* (2008) A korarchaeal genome reveals insights into the evolution of Archaea. *Proc. Natl Acad. Sci. USA*, **105**, 8102–8107.
19. Davies,D.R. and Hol,W.G.J. (2004) The power of vanadate in crystallographic investigations of phosphoryl transfer enzymes. *FEBS Lett.*, **577**, 315–321.
20. Slade,D. and Radman,M. (2011) Oxidative stress in *Deinococcus radiodurans*. *Microbiol. Mol. Biol. Rev.*, **75**, 133–191.
21. Akey,D., Martins,A., Aniukwu,J., Glickman,M.S., Shuman,S. and Berger,J.M. (2006) Crystal structure and nonhomologous end joining function of the ligase domain of *Mycobacterium* DNA ligase D. *J. Biol. Chem.*, **281**, 13412–13423.
22. Blasius,M., Buob,R., Shevelev,I.V. and Hubscher,U. (2007) Enzymes involved in DNA ligation and end-healing in the radioresistant bacterium *Deinococcus radiodurans*. *BMC Mol. Biol.*, **8**, 69.
23. Martins,A. and Shuman,S. (2004) An RNA ligase from *Deinococcus radiodurans*. *J. Biol. Chem.*, **279**, 50654–50661.
24. Trujillo,K.M., Yuan,S.F., Lee,E.Y. and Sung,P. (1998) Nuclease activities in a complex of human recombination and DNA repair factors Rad50, Mre11, and p95. *J. Biol. Chem.*, **273**, 21447–21450.
25. Martins,A. and Shuman,S. (2005) An end-healing enzyme from *Clostridium thermocellum* with 5′ kinase, 2′,3′ phosphatase, and adenylyltransferase activities. *RNA*, **11**, 1271–1280.
26. Hopfner,K.P., Karcher,A., Craig,L., Woo,T.T., Carney,J.P. and Tainer,J.A. (2001) Structural biochemistry and interaction architecture of the DNA double-strand break repair Mre11 nuclease and Rad50-ATPase. *Cell*, **105**, 473–485.
27. Keppetipola,N. and Shuman,S. (2005) Mechanism of the phosphatase component of *Clostridium thermocellum* polynucleotide kinase-phosphatase. *RNA*, **12**, 73–82.
28. Aniukwu,J., Glickman,M.S. and Shuman,S. (2008) The pathways and outcomes of mycobacterial NHEJ depend on the structure of the broken DNA ends. *Genes Dev.*, **22**, 512–527.